

PAPER

# A programmable metasurface for real time control of broadband elastic rays

To cite this article: Yangyang Chen *et al* 2018 *Smart Mater. Struct.* **27** 115011

View the [article online](#) for updates and enhancements.

# A programmable metasurface for real time control of broadband elastic rays

Yangyang Chen<sup>1</sup>, Xiaopeng Li<sup>1</sup>, Hussein Nassar<sup>1</sup>, Gengkai Hu<sup>2</sup> and Guoliang Huang<sup>1</sup> 

<sup>1</sup>Department of Mechanical and Aerospace Engineering, University of Missouri, Columbia, MO 65211, United States of America

<sup>2</sup>School of Aerospace Engineering, Beijing Institute of Technology, Beijing, 100081, People's Republic of China

E-mail: [huangg@missouri.edu](mailto:huangg@missouri.edu)

Received 6 July 2018, revised 21 August 2018

Accepted for publication 19 September 2018

Published 15 October 2018



CrossMark

## Abstract

Real-time engineering of elastic rays in solid materials is crucial for several applications relevant to active noise and vibration cancellation and to inverse methods aiming to either reveal or dissimulate the presence of foreign bodies. Here, we introduce a programmable elastic metasurface for the first time with sensing-and-actuating units, allowing to adapt and reprogram its wave control functionalities in real time. The active units behave following decoupled 'feedforward' sensor-to-actuator control loops governed by local transfer functions encoded into a digital circuit and offering highly flexible phase and amplitude engineering of transmitted and/or scattered waves. The proposed metasurface is concretized numerically and experimentally by achieving, for the first time, real-time tunable ray steering of flexural waves in a host plate. Various other significant demonstrations have been included to strongly illustrate the multifunctional adaptability of the design. In particular, one-way non-reciprocal blocking of waves is observed experimentally whereas skin cloaking of voids is tested numerically. Finally, operability across broad wave frequency ranges is demonstrated (5–45 kHz). The design will pave a new efficient way in the field of sensing and actuation of elastic waves.

Supplementary material for this article is available [online](#)

Keywords: programmable metasurface, elastic ray control, real-time wave control

(Some figures may appear in colour only in the online journal)

## 1. Introduction

Guided elastic or acoustic waves have been proven to provide superior methods in probing the mechanical properties of materials and imaging invasive objects across a range of scales from lab specimen and living tissues, to civil engineering structures and subterranean reservoirs [1]. Nonetheless, there exist challenging scenarios where the capabilities of conventional phased array techniques [2, 3] and metamaterial-based waveguides with spatially varying material properties [4–10] are not sufficient or extremely costly. These include cases where real-time and non-reciprocal asymmetric control of elastic/acoustic ray trajectories, be them linear or curved, blocked or amplified, is desired. Although a lot of efforts have

been devoted to active elastic/acoustic metamaterials to serve those purposes [11–20], the resulting designs still tend to be bulky, invasive and necessitate impractical use of complex control systems.

Metasurfaces, a new kind of artificial planar metamaterials, have recently emerged as powerful means to transform incident waves by creating arbitrarily shaped transmitted or reflected wavefronts [21]. The transformation is accomplished by arranging suitable field discontinuities on a flat interface. Remarkably, due to dimensionality in 2D space for instance, the number of units constituting a metasurface scales approximately as the square root of that necessary in a bulk metamaterial. This significant reduction in the number of constitutive units makes metasurfaces excellent substitutes for

bulk metamaterials offering thin designs with manageable control systems. The concept of metasurfaces has found a lot of interesting and unconventional applications in electromagnetic wave control [22–25] and subsequently spread to acoustics [26–30] and elasticity [31–33]. However, passive metasurfaces with non-configurable functions can only operate in narrow frequency bands, which significantly limits their use in practice [25].

On the other hand, active metasurfaces with reconfigurable functionalities have received considerable interests recently in optics and acoustics and became a rapidly growing field in material science and engineering [25, 30, 34–37]. For example, by introducing voltage-controlled varactors [25, 34] or diodes [35] into resonating meta-atom structures of electromagnetic metasurfaces, the effective index can be controlled locally along the metasurface to achieve the desired phase abrupt. A nonlinear reconfigurable metasurface was also proposed by blocking the incident acoustic wave and, at the same time, emitting a higher order harmonic transformed wave field [30, 37]. However, extensions of active acoustic metasurfaces to the control of elastic waves in solids are not straightforward and none of successful designs on active elastic metasurfaces are reported so far.

Motivated by these considerations, the present paper introduces a simple platform of a programmable elastic metasurface (see figure 1(a)) and experimentally demonstrates, for the first time, real-time reconfigurable and multifunctional control of flexural waves in plates. The proposed metasurface consists of a 1D array of self-sensing-and-actuating units composed of piezoelectric patches bonded on a plate, each unit being controlled by a simple digital circuit, which can be remotely coded through wireless communications. In the adopted paradigm, the local wave transmittance and phase profiles that encode the current functionality of the metasurface can be repeatedly tuned in real time with the programmed circuits to achieve different functionalities with quasi-instantaneous response times compared to the time period of the propagating waves. In this manner, real-time tunable wave steering and curvilinear trajectory adjustment are demonstrated experimentally. The functionalities that can be programmed into the metasurface are by no means limited to single ray path control and are extended to simultaneous multifunctional wave control. To further exemplify the range of functionalities that can be attained, an experimental demonstration of one-way non-reciprocal wave transmission is presented. In this configuration, the metasurface blocks waves incident in a given direction while amplifying waves incident in the opposite direction. The application of the metasurface to skin cloaking is illustrated numerically as well. Last, operability in broadband frequency ranges is investigated. The proposed concept of a programmable elastic metasurface should significantly enhance elastic wave control techniques in a way that will benefit the fields of structural health monitoring and ultrasonic imaging especially in complex heterogenous structures, not to mention active and unidirectional noise cancellation and stealth technologies.

## 2. Design principles

To construct the metasurface, a 1D periodic array of thin slits is delicately cut into a host steel plate (see figure 1(a)). Sensing and actuating beams are then formed between the slits. Each of the sensing beams is bonded with two identical piezoelectric patches placed symmetrically with respect to the metasurface whereas each actuating beam is bonded with one piezoelectric patch located at the mid-thickness of the metasurface. Sensing beams will extract the background incident wave signal based on which, through a ‘feedforward’ control loop, the actuating beams will generate coherent waves thus allowing, by constructive and/or destructive interference, to control both the phase and amplitude of the transmitted signal.

Sensors and actuators communicate through a digital-circuit control system (see figure 1(b)). In each unit cell, the two sensors are individually connected to two charge amplifiers and two low-pass band filters. The filtered voltage signals coming from the sensors contain contributions from both the incident wave and the coherent waves generated by the actuators. Subtracting the output signals of each pair of sensors yields an input signal, called  $V_{in}$ , where, due to mirror symmetry, the contribution of generated coherent waves has been eliminated and only the contribution of the background incident signal is retained. It should be mentioned that the subtraction operation not only removes intra-cell actuator-to-sensor feedback effects but further eliminates inter-cell effects as well. This decoupling ensures that the metasurface functionality can be programmed locally unit cell by unit cell and thus greatly reduces the complexity of the underlying electrical control system. Note that in general, scattering of waves by the piezoelectric patches at subwavelength scales is weak and will be ignored.

In the study, the Kirchhoff plate theory is employed, because the wavelength in the frequency range of interest to the metasurface is much larger than the thickness of the plate ( $\lambda/h \approx 18$  at 10 kHz), where the effect of the thickness shear deformation could be ignored. The governing equation of flexural waves in a homogeneous isotropic plate can be expressed as

$$D\nabla^2(\nabla^2 w) + \rho h \frac{\partial^2 w}{\partial t^2} = 0, \quad (1)$$

where  $\rho$  and  $h$  represent the mass density and thickness of the plate, respectively, and  $\nabla^2 = \frac{\partial^2}{\partial x^2} + \frac{\partial^2}{\partial y^2}$ ,  $D = \frac{Eh^3}{12(1-\nu^2)}$  with  $E$  and  $\nu$  being the Young’s modulus and Poisson’s ratio of the host plate material, respectively.

For the metasurface with deep subwavelength thickness, wave scattering from free boundaries due to cut slits can be ignored. The assumption has been verified by our numerical simulations with both normal and oblique incidences. The incident plane wave in the host plate and sensing and actuating beams is then assumed as

$$w_i = w_0 e^{ik(x \cos \theta + y \sin \theta)}, \quad (2)$$

where  $\theta$  represents the incident angle as shown in figure 2, the

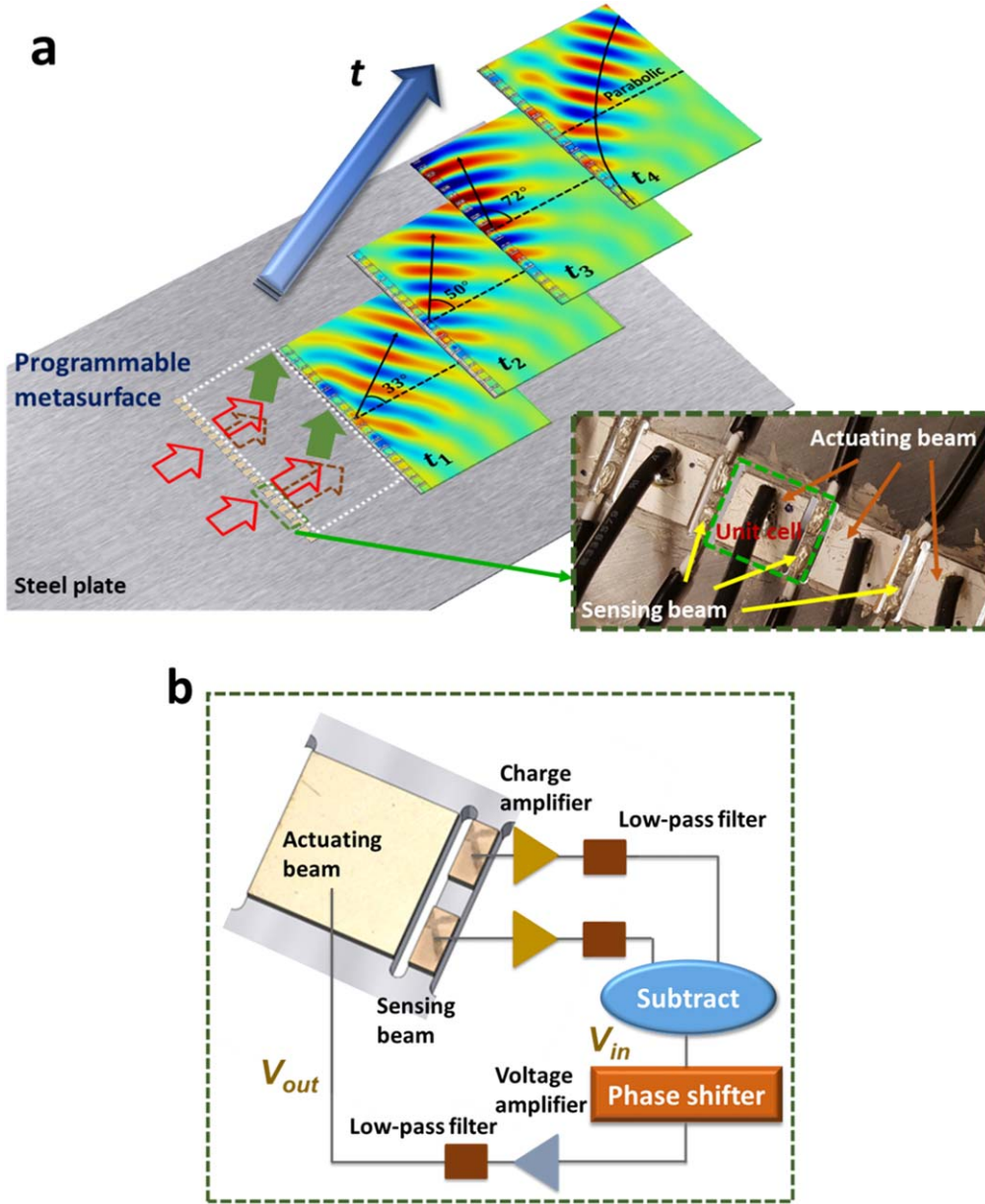


**Figure 1.** (a) Schematic of the programmable metasurface with an illustration of real-time tunable elastic ray control. Red, brown and green solid arrows represent incident, coherent and superposed total wave fields, respectively. By programming the digital circuits of the metasurface, wavefronts are shaped and tuned in real time. (b) Unit cell design of the programmable metasurface.

wavenumber  $k = \left(\frac{\rho h \omega^2}{D}\right)^{1/4}$  and  $w_0$  denotes the complex wave amplitude. It should be noted that the reflection due to the presence of surface-bonded piezoelectric plates are ignored because of their subwavelength dimensions and small impedance mismatch.

According to the Kirchhoff plate theory, the strain fields on the top electrodes of the piezoelectric sensors along  $x$ - and  $y$ -directions are written as

$$\varepsilon_x = k^2 \cos^2 \theta w_0 \tilde{h}_p e^{ik(x \cos \theta + y \sin \theta)}, \quad (3a)$$

$$\varepsilon_y = k^2 \sin^2 \theta w_0 \tilde{h}_p e^{ik(x \cos \theta + y \sin \theta)}, \quad (3b)$$

in which  $\tilde{h}_p$  represents the distance between the upper surface of the piezoelectric plate to the neutral plane of the sensor beam.

Here, we select a unit cell located at the origin. The voltage signal acquired from the charge amplifier connected to ‘Sensor 1’ (figure 2) can be expressed as

$$V_1 = \frac{Q_1}{C_0}, \quad (4)$$

where the free charge on the electrode  $Q_1 = \int_{S_1} -e_{31}(\varepsilon_x + \varepsilon_y) dS$ , with  $e_{31}$  being the piezoelectric constant, and  $C_0$  denotes the reference capacitance in the charge amplifier. It should be mentioned that this signal only contains the incident wave component. The coherent wave components generated by metasurface actuators will be canceled out by the subtraction operation between the two sensors.

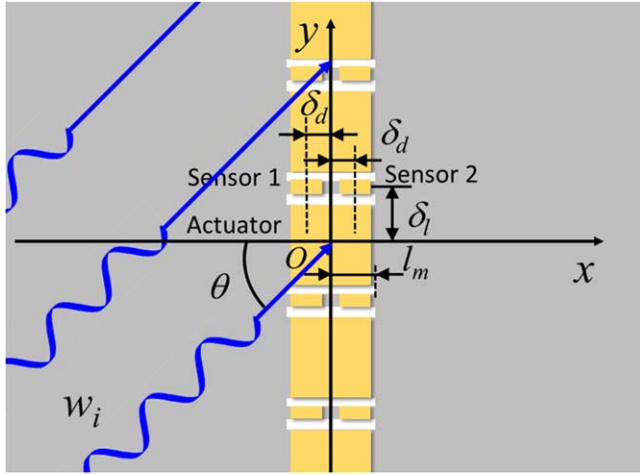


**Figure 2.** Schematic of the harmonic wave analysis of the metasurface with oblique incidence.

Inserting equation (3) into (4), we have

$$V_1 = \kappa_s A w_0 e^{ik(-\delta_d \cos \theta + \delta_l \sin \theta)}, \quad (5)$$

where  $\kappa_s = \frac{e_{31} \bar{h}_p}{C_p^T \cos \theta \sin \theta} \left( e^{\frac{ikh_s \cos \theta}{2}} - e^{-\frac{ikh_s \cos \theta}{2}} \right) \left( e^{\frac{ikb_s \sin \theta}{2}} - e^{-\frac{ikb_s \sin \theta}{2}} \right)$  and  $A = \frac{C_p^T}{C_0}$  denoting the amplification ratio of the charge amplifier with  $C_p^T$  being the capacitance of the piezoelectric sensor at constant stress. Similarly, the voltage signal acquired from the charge amplifier connected to the ‘Sensor 2’ can be written as

$$V_2 = \kappa_s A w_0 e^{ik(\delta_d \cos \theta + \delta_l \sin \theta)}. \quad (6)$$

According to the design principles, the input signal,  $V_{in}$ , attained from the two sensors is

$$V_{in} = V_1 - V_2 = -2i\kappa_s A w_0 \sin(k\delta_d \cos \theta) e^{ik\delta_l \sin \theta}. \quad (7)$$

The output signal from the electrical control system,  $V_{out} = HV_{in}$ , is then applied across the corresponding actuator in the metasurface unit cell, which generates two coherent waves propagating to both sides of the metasurface. Here, all unit cells are encoded with the same transfer function. The wave field in the right-hand side of the metasurface, which is proportional to the voltage,  $V_{out}$ , can be assumed as

$$w_a = i\kappa_a V_{out} e^{ik(x \cos \theta + y \sin \theta)}, \quad x > l_m, \quad (8)$$

where  $\kappa_a$  is defined as the electromechanical coupling coefficient of the piezoelectric actuator that will be determined numerically due to complex geometries and  $\theta$  is valid from  $-60^\circ$  to  $60^\circ$ . Finally, the total transmitted wave field is

$$w_t = [1 + 2\kappa_a \kappa_s A H \sin(k\delta_d \cos \theta) e^{ik\delta_l \sin \theta}] \times w_0 e^{ik(x \cos \theta + y \sin \theta)}. \quad (9)$$

It can be found from equation (9) that both the amplitude and phase of the transmitted wave can be independently controlled by the transfer function,  $H$ . The local transfer function defined as the ratio of the output voltage applied across the actuator to the input signal  $V_{in}$  summarizes the function of a single unit

cell. For transmission-type metasurfaces with only phase engineering, the transmittance is usually designed to be unitary, therefore,

$$H = \frac{e^{i\phi} - 1}{2\kappa_a \kappa_s A \sin(k\delta_d \cos \theta) e^{ik\delta_l \sin \theta}} = C(e^{i\phi} - 1), \quad (10)$$

in which  $\phi$  is the desired phase abrupt induced by the metasurface and the amplification ratio  $C = 1/[2\kappa_a \kappa_s A \sin(k\delta_d \cos \theta) e^{ik\delta_l \sin \theta}]$ .

As a special case, for the metasurface with normal incidence, the transfer function will become

$$H = \frac{e^{i\phi} - 1}{2\kappa_a \kappa_s A \sin(k\delta_d)} = C(e^{i\phi} - 1), \quad (11)$$

where  $C = 1/[2\kappa_a \kappa_s A \sin(k\delta_d)]$ . Due to the geometric complexity, the constant,  $C$ , is extremely difficult to be determined analytically. A numerical approach is then applied.

In order to achieve the transfer function of equation (10), phase shifter and voltage amplification circuits are constructed and are shown in figure 1(b). Note that a unitary transmittance does not mean that no extra elastic energy is radiated in the direction of the incident wave. In fact, the phase jump of the transmitted wave is purely caused by the elastic energy input from the electrical domain. For the transmission-type metasurface, only the transmitted half of that energy is useful whereas the backscattered half is lost.

It has already been noticed that the internal amplification factor  $C$  (equation (2)) implemented in the electrical system of the metasurface depends on the incident wave angle. However, for practical applications, the incident angle is usually unknown for the metasurface. To address the issue, two approaches are further quantitatively analyzed to illustrate the applicability of the metasurface under oblique incidences including: (1) the amplification factor for the normal incidence  $C(\theta = 0) = C_0 = 1/[2\kappa_a \kappa_s A \sin(k\delta_d)]$  is used by ignoring effects of oblique angles, which will be discussed in section 4.1; (2) a modified control design in the electric system is suggested to exactly compensate the effect of the oblique angle on the metasurface, which will be discussed in section 4.2.

Piezoelectric-coupled 3D numerical simulations were performed to validate the phase control abilities of a single unit cell at 10 kHz (see figure 3(a)). Therein, the top and bottom boundaries of the simulated domain are set to be symmetric and constant  $C_0$  is determined numerically. Geometric parameters are illustrated in figure 3(a) with the values listed in table 1. The thickness of the host steel plate is selected as 3.0 mm and the thicknesses of sensor and actuator patches are 1.1 mm and 1.0 mm, respectively. As shown on the top portion in figure 3(b), the top and bottom boundaries of the simulated domain are set to be symmetric. The out-of-plane displacement wave field in figure 3(b) illustrates that the phase change introduced into the transmitted wave is almost exactly the same, with the phase,  $\phi$ , prescribed in the simulation by using equation (11), where  $\phi = 0, \pi/3, 2\pi/3, \pi, 4\pi/3, 5\pi/3, \text{ and } 2\pi$ , respectively. It can also be found from the figure that the amplitudes of transmitted waves among all

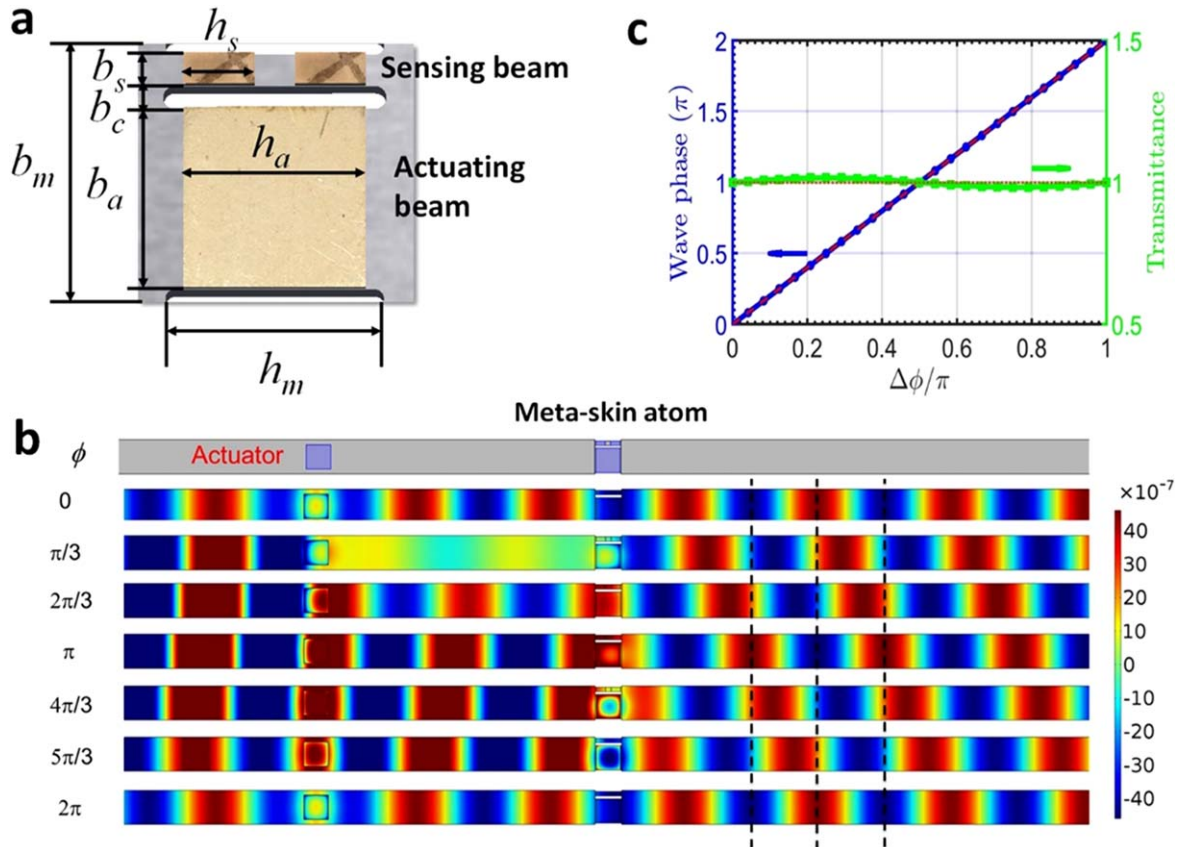


**Figure 3.** (a) Geometric parameters of the unit cell of the transmission-type programmable metasurface; (b) out-of-plane displacement wave field manipulated by the programmable metasurface with different phase abrupt in simulations; (c) wave transmittance and induced phase jump determined analytically and numerically for a single unit cell in a quasi-1D setting.

**Table 1.** Geometric parameters of the transmission-type programmable metasurface.

$b_s$	1.75 mm	$b_m$	14.0 mm	$h_s$	3.9 mm	$h_m$	11.0 mm
$b_c$	1.25 mm	$b_a$	10.0 mm	$h_a$	10.0 mm		

the cases are almost identical. Figure 3(c) summaries this behavior, where analytical predictions based on equation (10) (dashed lines) as well as simulated values (solid curves) of the phase and transmittance are plotted against one another and show satisfactory agreement. The results illustrate how full phase control of the transmitted wave from 0 to  $2\pi$  altogether while uniformly maintaining nearly unitary transmittance can be achieved simply by programming the electrical system within a unit cell. The small fluctuations in the simulated transmittance are caused by weak reflections due to the presence of sensors and actuators on the plate.

### 3. Sample fabrications and experimental setup

Figure 4(a) shows the fabricated metasurface sample as well as the experimental setup for wave field measurements. To fabricate the corresponding sensing and actuating beams, a periodic array of thin slits was cut by a fiber laser cutting machine on a steel plate with the dimensions being

$1 \text{ m} \times 2 \text{ m} \times 3 \text{ mm}$  (see figure 4(a)). An array of piezoelectric plates (APC 850, APC 855) was then bonded on the surfaces of those sensing and actuating beams by a conductive epoxy (Chemtronics) to comprise those sensors and actuators of a metasurface with 20 unit cells (see the inset figure in the right side of figure 4(a)). Another array of piezoelectric plates (APC 850) was bonded to the left-hand-side 120 mm away from the metasurface to generate normally incident plane flexural waves (see the inset figure in the left side of figure 4(a)). To produce an incident plane wave, a 10-peak tone burst signal with central frequency being 10 kHz was generated by a Tektronix AFG3022C arbitrary waveform generator and amplified by a Krohn-Hite high voltage power amplifier, which was finally applied across the actuator array in the left-hand side of the metasurface. The transmitted out-of-plane velocity wave field in the scanning area was measured by a Polytec PSV-400 scanning laser Doppler vibrometer (see figure 4(a)).

In our metasurface design, each of the metasurface unit cells had an individual circuit control system which was divided into several small parts with specifically assigned functions, i.e. charge and voltage amplifiers, low-pass filters and microcontrollers. All the circuits were fabricated on printed circuit boards, and finally assembled into two large boards for all the 20 unit cells. Figure 4(b) shows the fabricated circuits for 10 unit cells, where all the analog circuits

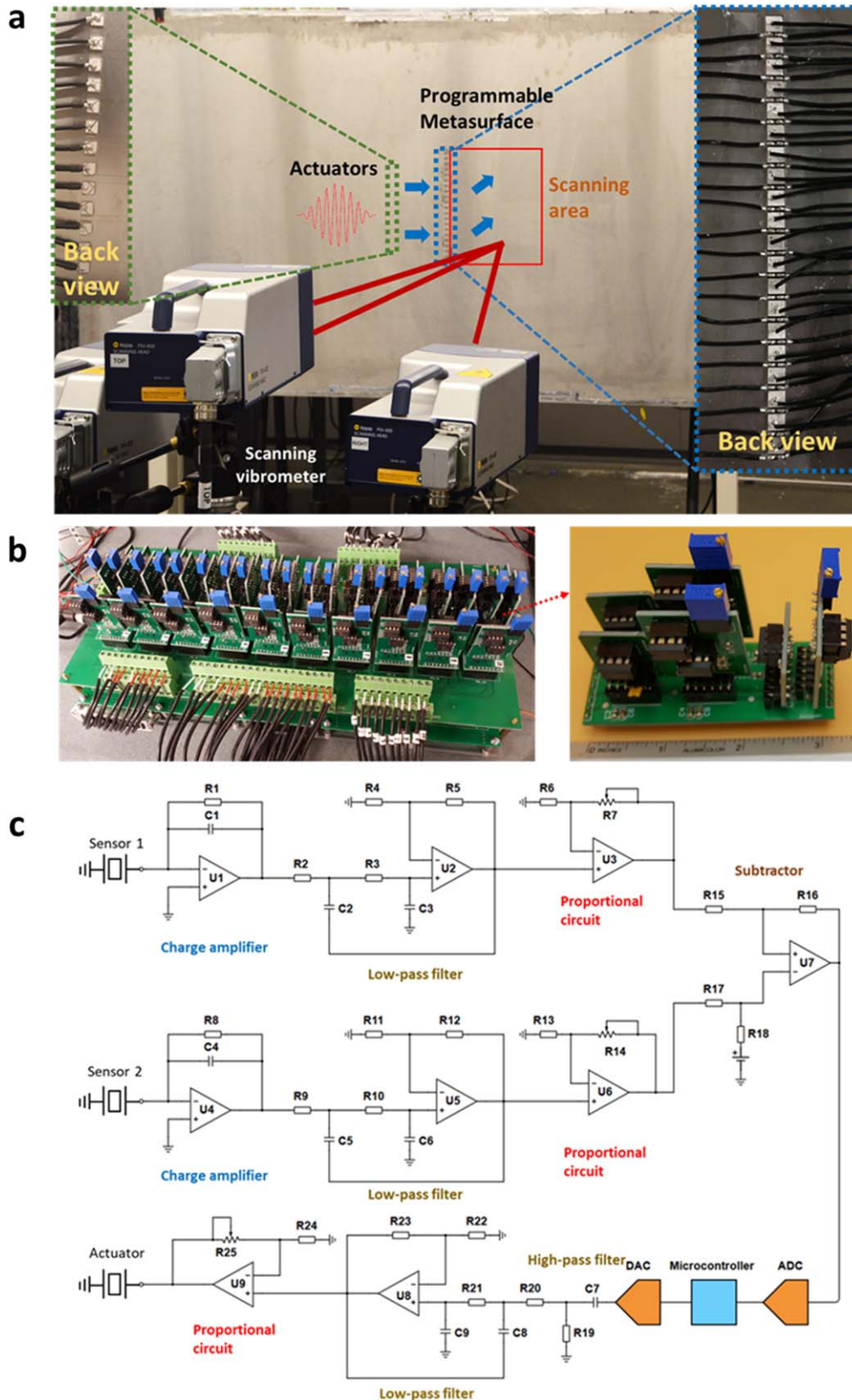


**Figure 4.** (a) Experimental setup of the programmable metasurface; (b) photos of the fabricated control circuits; (c) the diagram of the metasurface control circuit for one unit cell.

**Table 2.** Circuit parameters of the fabricated control circuit system.

$R1, R8$	1 M $\Omega$	$R2, R3,$ $R9, R10,$ $R20, R21$	3 k $\Omega$	$R4-R6,$ $R11-R13,$ $R15-R18,$ $R22-R24$	1 k $\Omega$	$R19$	14.7 k $\Omega$
$R7, R14$	0–10 k $\Omega$	$R25$	0–100 k $\Omega$	$C1, C4$	100 pF	$C2, C3, C5-C9$	2 nF
$U1-U7$	OPA604	$U8, U9$	OPA445	Micro-controller		STM32F405	

were placed on the upper layer and all the digital circuits were located on the lower layer. In particular, the diagram of the control circuit in a metasurface unit cell is shown in figure 4(c) with the circuit parameters given in table 2. Three low-pass filters were implemented into a metasurface unit cell. In the circuit design, two second-order Sallen-Key low-pass filters connected to two sensors, respectively, were used to remove high-frequency noises from the sensing signals. Here, the cutoff frequency was tuned to 26.5 kHz such that signals sending to the microcontroller can possess high signal-to-noise-ratios, and therefore the original sensing signal centered at 10 kHz would not be distorted. In addition, another second-order Sallen-Key low-pass filter was connected to the actuator aimed to suppress high-frequency noises from the microcontroller due to the discrete sampling. The cutoff frequency was still tuned to 26.5 kHz for the same reason. Last, it should mention that the sensing feedback components from actuating have been theoretically suppressed through the subtraction operation. However, in real experiments, there still exist weak sensing feedback components from actuating caused by the fabrication errors, circuit inaccuracies and boundary reflections. Those components could become relatively strong and induce high-frequency unstable modes. The low-pass filters can also efficiently eliminate those unwanted components and stabilize the entire control system.

## 4. Results and discussions

### 4.1. Real-time tunable steering of rays

The key component of wave manipulation circuits is the transfer function profile  $H = H(y)$  controlling the wave transmission properties of the metasurface as a whole where  $y$  is the local position of the individual unit cell along the metasurface. For instance, the generalized Snell's law dictates that the refraction angle  $\theta_t$  of the transmitted wave is related to the phase gradient  $\frac{\Delta\phi}{\Delta y}$  according to  $\sin \theta_t = \frac{\Delta\phi}{k\Delta y}$  with normal incidence [21]. As a special case, a linear phase profile implies that the transmitted wave has uniform and rectilinear ray paths. In other words, the refraction angle  $\theta_t$  can also be determined by  $\sin \theta_t = \frac{\lambda}{\Delta d}$ , where  $\Delta d$  is the distance along the metasurface across which the prescribed phase changes by  $2\pi$  and  $\lambda$  is the operating wavelength. To achieve the linear phase jump profile  $\phi(y)$ , i.e.  $\phi_1 = 0, \phi_2 = \frac{\pi}{4}, \phi_3 = \frac{\pi}{2}, \phi_4 = \frac{3\pi}{4}, \phi_5 = 2\pi, \phi_6 = \frac{\pi}{4}, \dots$  for unit cells from #1 to #20 with  $\Delta d = 56$  mm,  $H(y)$  needs to be programmed

locally, one unit cell by one unit cell, based on equation (11). In experimental testing, each unit cell in the metasurface has an independent circuit control system with a microcontroller and analog circuits connected to two sensors and one actuator, as shown in figure 4(c). The transfer function  $H$  of each unit cell defining the ratio of the output signal applied on the actuator to the input signal on the microcontroller is then locally programmed by both coding the microcontroller and tuning the potentiometer in the voltage amplifier connected to the actuator. In particular, the amplification factor  $C_0$  in the transfer function is determined through proper combinations of amplification ratios in charge and voltage amplifiers in the analog circuits. The term,  $(e^{i\phi} - 1)$ , in the transfer function  $H$  is implemented in the microcontroller, where the phase change is produced through coding the time delay between input and output signals of the microcontroller. The time delay in ADC, DAC, sampling and low-pass filters are also considered in the program. During the first three time intervals (see figures 5(a)–(c)), a uniform  $\Delta d$  is prescribed and changed from 98 to 70 and then to 56 mm, through coding the term,  $(e^{i\phi} - 1)$ , in each of the microcontrollers of the 20 metasurface unit cells. By programming phase profiles of the metasurface, the refraction angle of the transmitted wave can be steered from  $33^\circ$  to  $50^\circ$  and then to  $72^\circ$  in real time. The plots show that numerical and experimental results agree well and that steering angles coincide. Moreover, the possibility for programming nonlinear phase profiles offers the possibility to steer the transmitted ray paths according to curved trajectories. All other things being equal, in the fourth time interval, the phase profile along the metasurface is changed from a linear one to the one given by  $\phi = \frac{\pi a^2}{2\lambda} \ln[y + \sqrt{y^2 + (a^2/4)^2}]$  with  $a = 18.67$  mm in order to realize parabolic transmitted ray paths. In figure 5(d), numerical and experimental tests demonstrate the phenomenon. Although the real-time tunable wave steering has been demonstrated in acoustics [30], such extreme examples of real-time control of elastic waves based on simple programmable digital circuits have never been demonstrated before and should offer new possibilities in the field of structural health monitoring and ultrasonic imaging especially in complex heterogenous structures.

### 4.2. Applicability under oblique incidences

First, the dependence of the amplification factor  $C$  on the oblique incidence is investigated for the proposed metasurface in figure 5 by quantitatively calculating the amplitudes and phase angles of  $C/C_0$  with different incident angles as

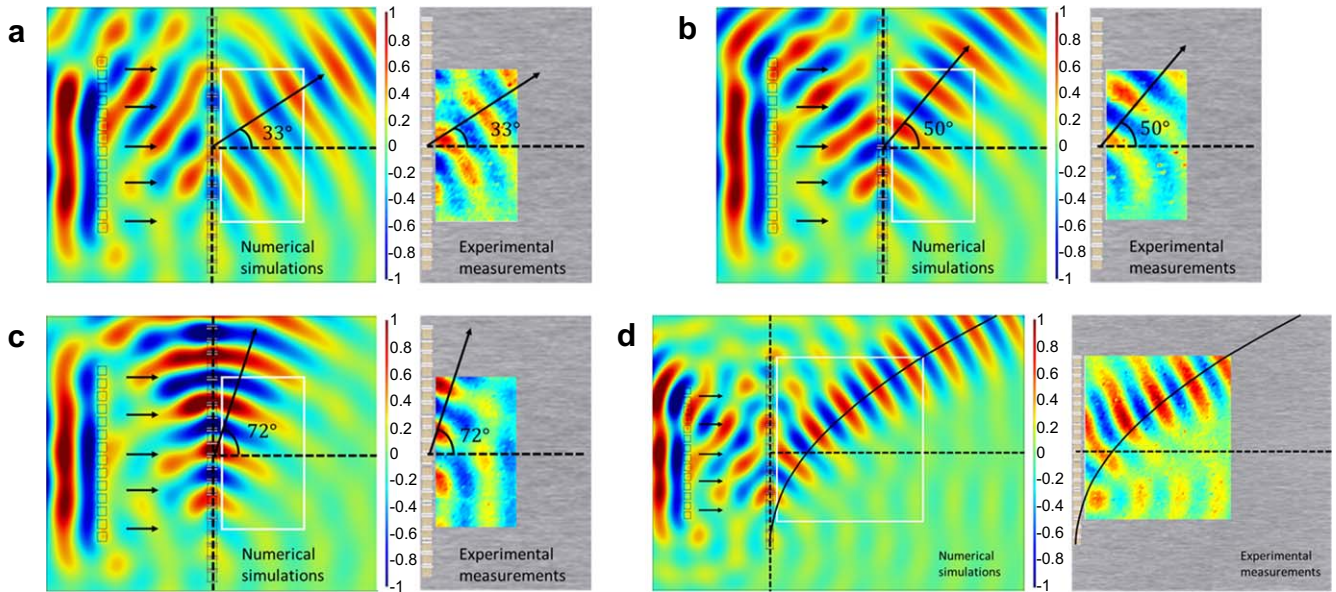


**Figure 5.** Real-time tunable steering of elastic rays. (a)–(d) Numerically simulated and experimentally measured out-of-plane velocity fields manipulated by the metasurface programmed with different phase profiles during different time intervals: (a) steering elastic rays to  $33^\circ$  during the first time interval; (b) steering elastic rays to  $50^\circ$  during the second time interval; (c) steering elastic rays to  $72^\circ$  during the third time interval; (d) achieving a parabolic ray path during the fourth time interval. In all cases, the right-going plane incident wave is generated by an array of piezoelectric patches. On the numerical plots, the regions framed in white correspond to zones where experimental measurements were obtained. Black arrows and curve represent the desired elastic ray direction and trajectory determined analytically.

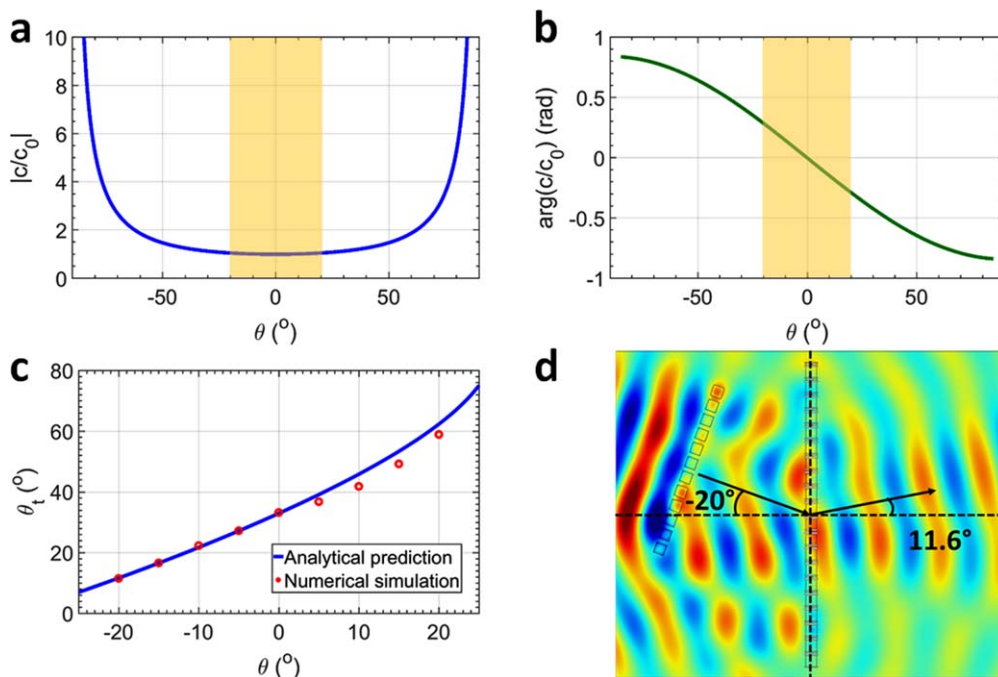


**Figure 6.** Applicability of the programmable metasurface with the amplification factor  $C = C_0$  under oblique incidences. (a), (b) The amplitude (a) and phase angle (b) of  $C/C_0$  under different incident angles; (c) comparison of numerically calculated and analytically predicted refractive angles of transmitted waves of the metasurface under different incident angles, where the amplification factor  $C = C_0$ ; (d) numerically simulated out-of-plane displacement wave field manipulated by the metasurface with the amplification factor  $C = C_0$  under  $-20^\circ$  incidence.

shown in figures 6(a) and (b), respectively. It is seen that when the incident wave angle is between  $-20^\circ$  and  $20^\circ$  (shaded areas), variations of both the amplitude and phase angle of  $C/C_0$  are very small, indicating a weak dependency of the internal amplification factor  $C$  on small incident angles.

This also implies that the amplification factor  $C_0$  could be robust for small angles of incidences by ignoring incident angle effects. Then, the wave steering performance of the proposed metasurface with the internal amplification factor  $C = C_0$  are quantitatively evaluated for different oblique

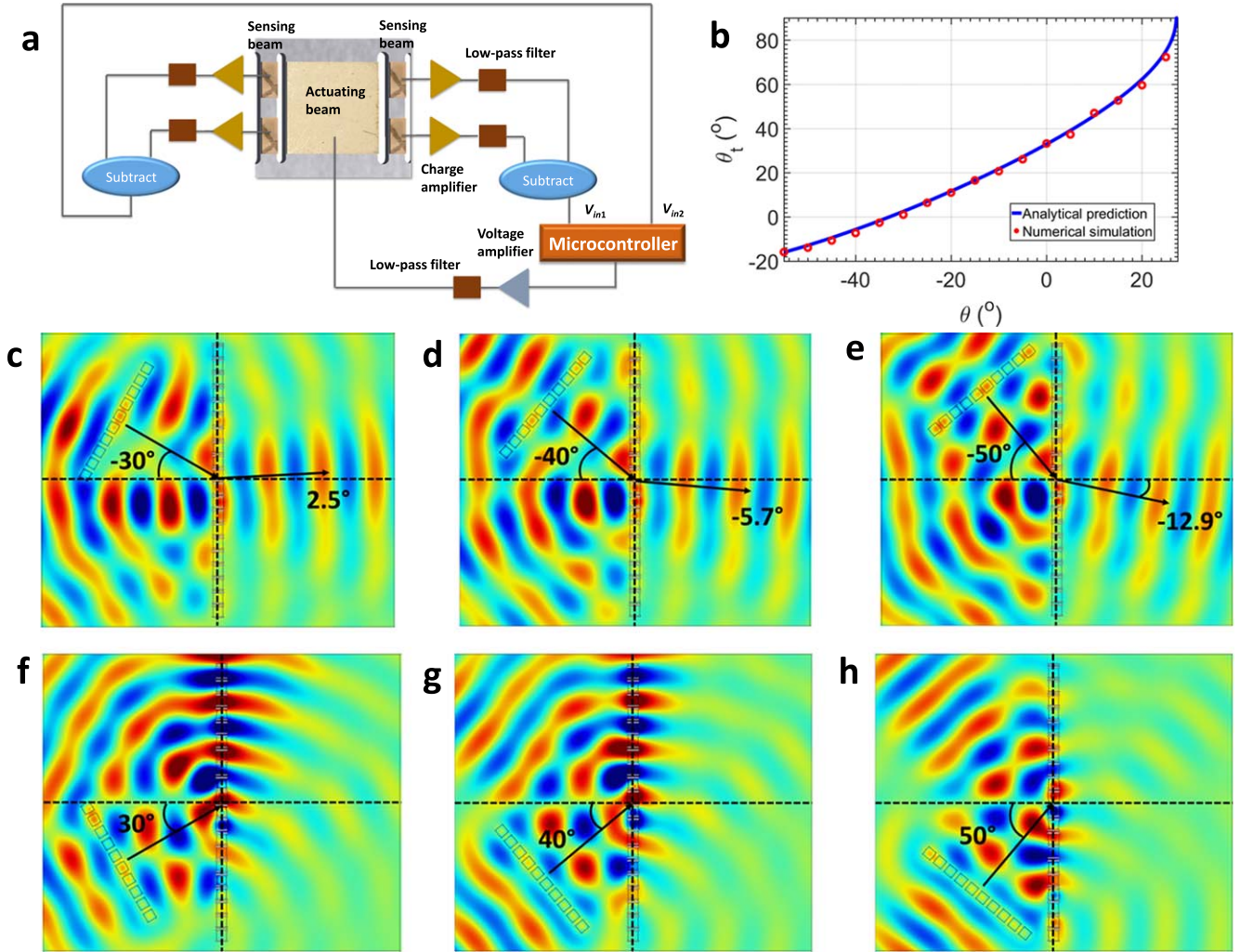


**Figure 7.** (a) Schematic of the modified electrical system of the metasurface with the amplification factor  $C$  for large-angle incidences; (b) comparison of numerically calculated and analytically predicted refractive angles of transmitted waves of the modified metasurface with the amplification factor  $C$  under different oblique incidences; (c)–(h) numerically simulated out-of-plane displacement wave fields manipulated by the modified metasurface with the amplification factor  $C$  under (c)  $-30^\circ$ , (d)  $-40^\circ$ , (e)  $-50^\circ$ , (f)  $30^\circ$ , (g)  $40^\circ$  and (h)  $50^\circ$  incidences.

incidences as shown in figure 6(c), where the controlled phase profile along the metasurface is the same as those in figure 5(a). It is found that numerically calculated refracted angles have a very good agreement with values analytically predicted according to the generalized Snell's law, when the oblique incident angle is between  $-20^\circ$  and  $20^\circ$ . The out-of-plane displacement wave field manipulated by the metasurface with the amplification factor  $C = C_0$  is also shown in figure 6(d) under  $-20^\circ$  incidence. For this case, the steered wave field is continuous with all the wave energy in the desired direction. Therefore, it can be concluded that the metasurface with amplification factor  $C = C_0$  should be applicable for the oblique incidences from  $-20^\circ$  to  $20^\circ$ .

#### 4.3. Programmable metasurface with an amplification factor considering incident angles

For large angles of incidences, the incident angle should be considered in transfer functions. To better serve this purpose, a modified electrical system design as shown in figure 7(a),

which can automatically determine the incident angle by the unit cells themselves is proposed and examined numerically. In the modified design, the electrical system includes additional connection from the sensing pair at the other side of the actuating patch. In this way, one sensing pair will be shared by two adjacent unit cells, and one microcontroller will have two input signals,  $V_{in1}$  and  $V_{in2}$ , from which the incident angle of a harmonic incident wave is determined as

$$\theta = \arcsin\left[\frac{\arg(V_{in1}) - \arg(V_{in2})}{kb_m}\right], \quad (12)$$

and will be used in the amplification factor  $C$  in equation (10).

To validate the design, we examine wave steering performances of the modified metasurface under oblique incidences in the range from  $-55^\circ$  to  $55^\circ$ , which is comparable to the ranges investigated in state-of-the-art passive acoustic or elastic metasurfaces. Figure 7(b) shows the numerically simulated and analytically predicted refractive angles of the modified metasurface with the internal amplification factor  $C$  under the same phase profile in figure 5(a). Very good

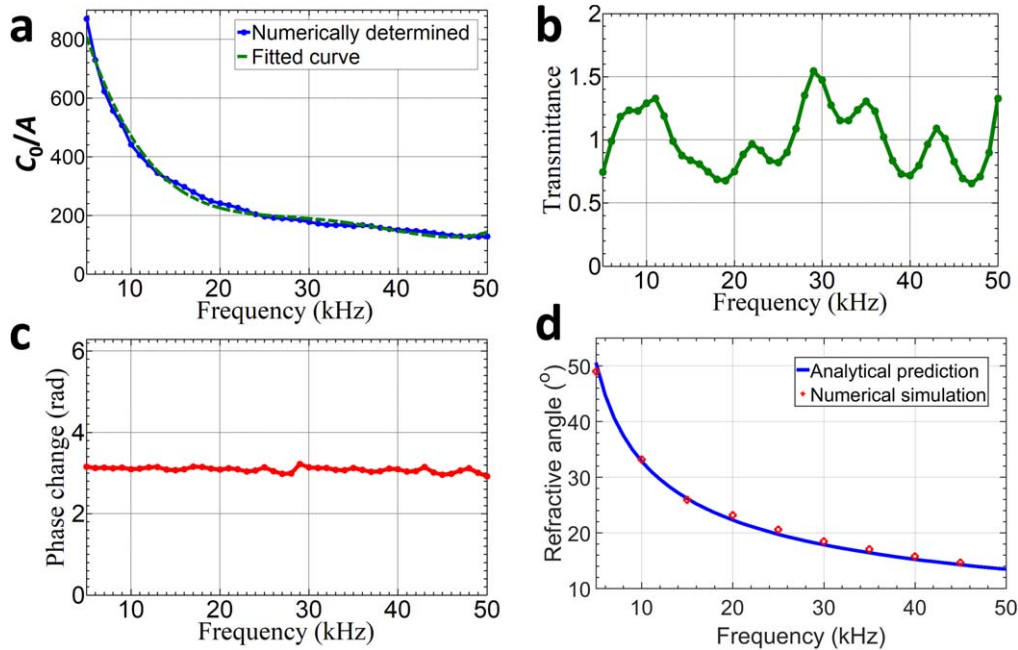


**Figure 8.** Broadband operability of the programmable metasurface. (a) Amplification ratio of the transfer function,  $C/A$ , determined numerically at different frequencies and its numerically fitted fourth order curve; (b) wave transmittance induced by the metasurface with the fitted fourth order transfer function; (c) wave phase change induced by the metasurface with the fitted fourth order transfer function; (d) numerically calculated and analytically predicted refractive angles of transmitted waves from the metasurface at different frequencies with the frequency-adaptive amplification factor.

agreement has been clearly observed from  $-55^\circ$  to  $25^\circ$ . The out-of-plane displacement wave fields manipulated by the modified metasurface are also illustrated in figures 7(c)–(e) under  $-30^\circ$ ,  $-40^\circ$  and  $-50^\circ$  incidences, respectively. As shown in the figures, all the transmitted energy is almost steered to their desired directions, which are predicted by the generalized Snell's law.

In addition, the out-of-plane displacement wave fields under  $30^\circ$ ,  $40^\circ$  and  $50^\circ$  incidences are also investigated in figures 7(f)–(h), respectively. It is found that under the same phase profile in figure 5(a), the transmitted waves in all three cases become purely evanescent indicating that only the fundamental order mode is preserved and is totally reflected. In contrast, passive designs cannot operate for wave blocking in this regime as they usually generate higher order refracted waves. However, all the higher order refractive waves are suppressed by our programmable metasurface.

#### 4.4. Broadband tunability

While operating at a subwavelength scale, the metasurface does not suffer from any frequency limitations. Note however that the programmed transfer functions are themselves frequency-dependent since the electromechanical coupling coefficient as well as the wavenumber vary with frequency (equation (10)). In particular, figure 8(a) shows the numerically determined profile of the amplification ratio  $C_0/A$  of the transfer function with respect to frequency (blue solid curve). Then, it can be seen that larger amplification ratios are required at lower frequencies than at higher ones, mainly because the electromechanical coupling coefficient  $\kappa_s \kappa_a$  and

wavenumber  $k$  are much smaller at lower frequencies than at higher frequencies. The dependency of the amplification ratio on frequency (see figure 8(a)) can be accurately compensated for by a fourth order function (green dashed curve). The wave transmittance and phase change induced by the metasurface unit cell with this fitted fourth order amplification ratio are shown in figures 8(b) and (c), where the phase  $\phi$  is prescribed as  $\pi$ . It can be seen that the phase jump strictly follows the prescribed values whereas transmittance present some limited fluctuations that will not significantly affect the performance of the metasurface. As an example, ray steering for the case shown in figure 5(a) is demonstrated in figure 8(d) at different frequencies from 5 to 45 kHz, where the refractive angles are in good agreement with the values predicted according to the generalized Snell's law [21]. Therein, the refraction angle is changed due to the dependency of the wavelength on frequency. Numerically simulated wave fields from 5 to 50 kHz are also shown in figure 9. It can be observed that the programmable metasurface has satisfactory wave steering performance for frequencies below or around 45 kHz (figures 9(a)–(e)). In these cases, the numerical results agree very well with the analytically predicted refraction angles (white arrows). It must be noted that the wave steering performance at 50 kHz (figure 9(f)) is slightly degraded as wavelengths become comparable to the thickness of the metasurface. Going beyond 50 kHz will necessitate the use of a metasurface by reducing the size of the unit cell. It should be noted that the results presented in figures 8 and 9 are for the single frequency cases sweeping over a range of frequencies. Most of literatures claiming broadband metasurfaces are based on the extrapolation of multiple narrow-

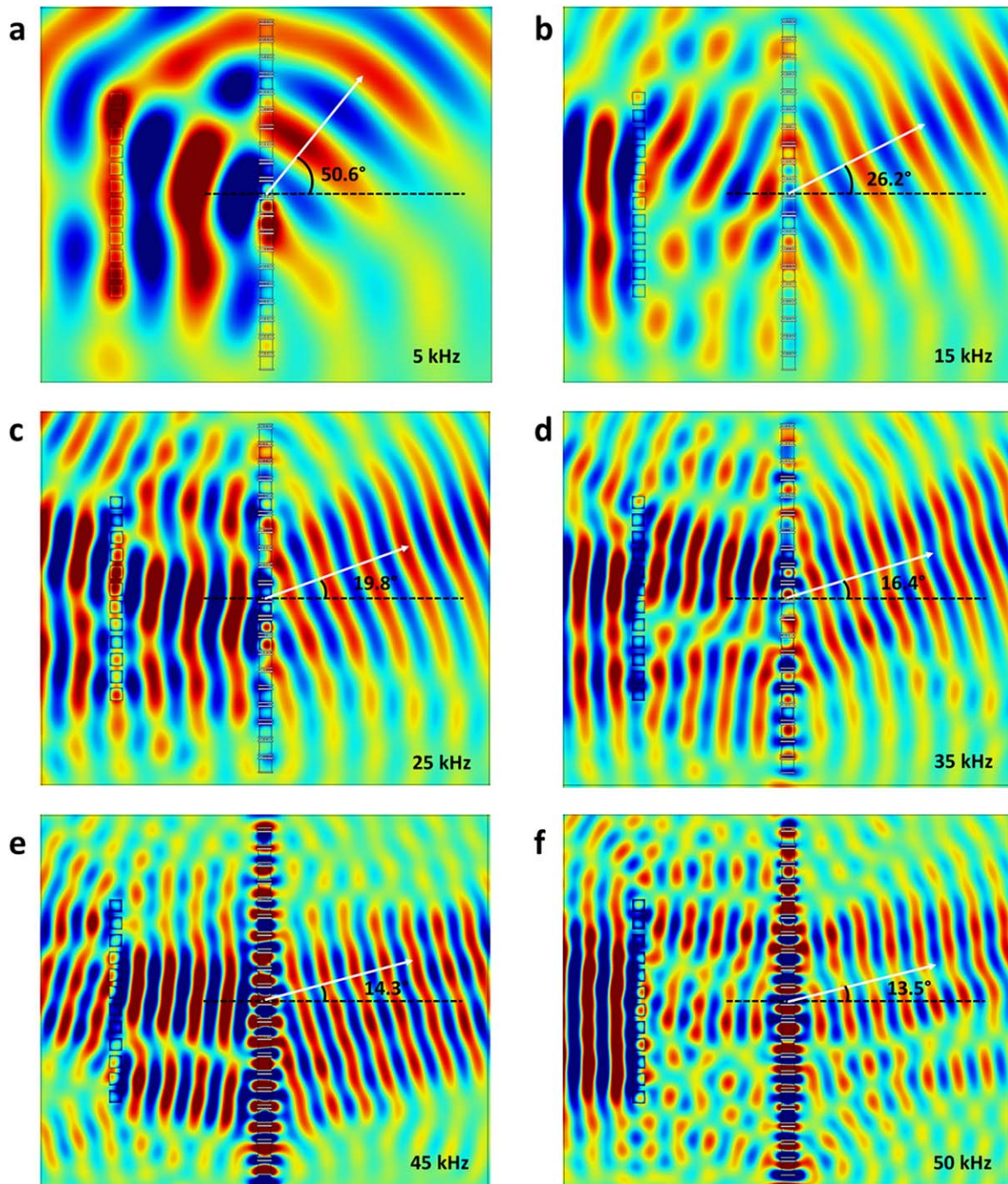


**Figure 9.** Numerically simulated normalized displacement field of the wave steering with the programmable metasurface at different frequencies: (a) 5 kHz; (b) 15 kHz; (c) 25 kHz; (d) 35 kHz; (e) 45 kHz; (f) 50 kHz.

band experimental or numerical results [33, 38–42]. The linear character of the flexural waves then allows us to safely claim that our metasurface can operate for broadband signals as long as their bandwidth is supported by the range 5–45 kHz. However, in practice, we face some difficulties to realize the transfer function  $H$  experimentally with the current hardware for broadband wave signals. As addressed before, the amplification factor  $C_0$  in the transfer function  $H$  should be a fourth-order function of the frequency (figure 8(a)), which can be coded into microcontrollers through IIR filters. During our experimental tests, it was found that the sample

frequency of the current microcontrollers was lowered to 41.6 kHz, which makes it impossible for the signal processing in the frequency range of interest to the metasurface. The experimental demonstration of a broadband metasurface will be conducted in our future study.

#### 4.5. Multifunctional transfer functions

It is worth mentioning that the functionalities of the programmable metasurface can be superposed by appropriately ‘summing’ the transfer functions of each functionality, as

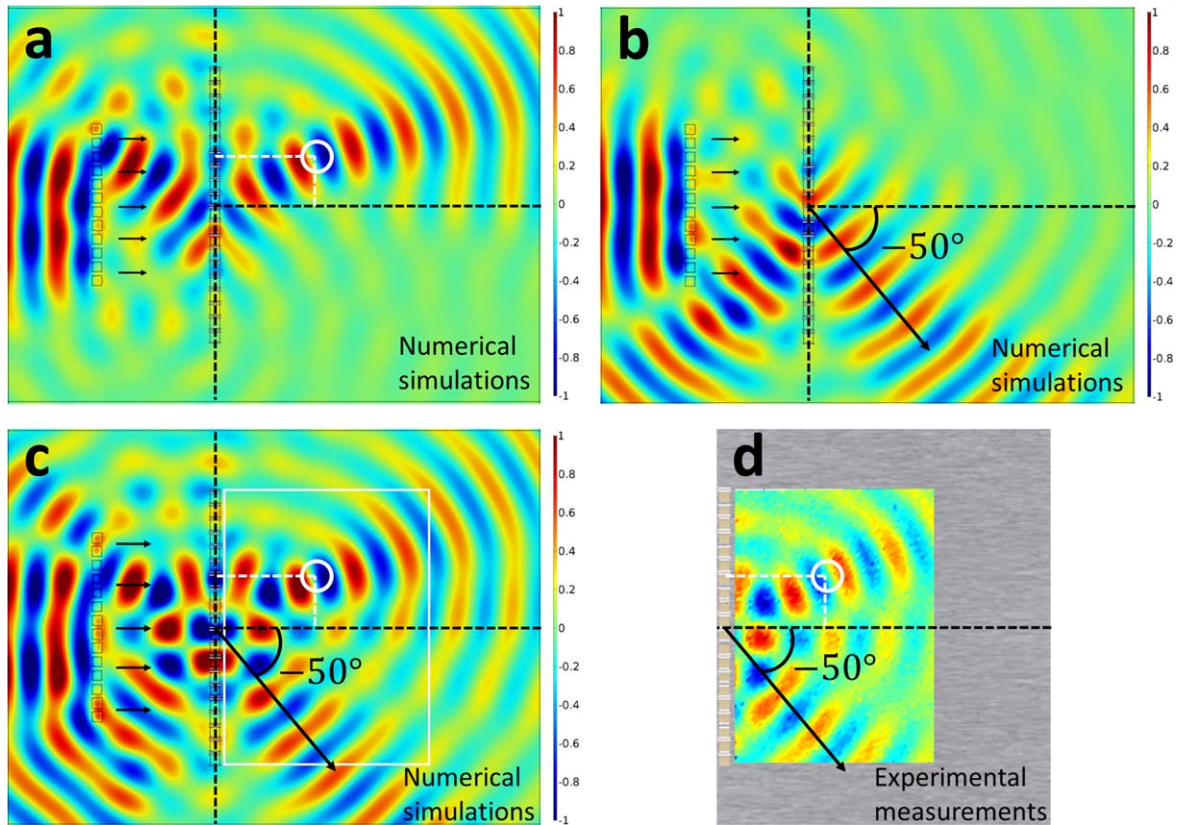


**Figure 10.** Simultaneous focusing and steering. (a), (b) Simulated normalized out-of-plane displacement fields manipulated by the metasurface encoded with single phase profile functions: (a) focusing elastic rays at  $x_0 = 100$  mm,  $y_0 = 50$ ; (b) steering elastic rays to  $-50^\circ$ . (c), (d) Numerically simulated and experimentally measured out-of-plane velocity fields manipulated by the metasurface encoded with the superposition of the focusing and steering transfer functions of (a) and (b). Wave focusing and steering are then achieved simultaneously: the plot of (c) is identical to the superposition of the two plots (a) and (b).

those demonstrated in acoustics before [30]. Given the phase profile necessary for steering  $\phi^{(1)}$  specified for  $\Delta d = 70$  mm, wave focusing can be achieved thanks to another phase profile  $\phi^{(2)} = \frac{2\pi}{\lambda}[\sqrt{x_0^2 + (y - y_0)^2} - x_0]$ , where  $x_0$  and  $y_0$  are the coordinates of the focal point (white circle on figure 10(a)); therein  $x_0 = 100$  mm and  $y_0 = 50$  mm). Numerical results shown in figures 10(a) and (b) confirm that each of these profiles achieve its intended functionality predicted analytically. Now, by combining the two phase profiles into a single new transfer function  $H = C(e^{i\phi^{(1)}} + e^{i\phi^{(2)}} - 1)$ , wave focusing and steering can be achieved simultaneously in order to, say, form two images, one close and one distant, of one source. Figures 10(c) and (d) demonstrate the simulated and experimentally measured wave fields with the new transfer function. It is found that the incident wave can be focused and steered, simultaneously, without any fading. Here, the extra elastic energy generated is extracted from the electric infrastructure. Programmed electrical and elastic power exchange can be utilized in other cases of elastic wave control as well.

#### 4.6. Enhanced imaging of a point source

By leveraging other transfer functions that channel more electrical energy, the convergent field can be amplified so as to enhance the intensity of the image. By combining both phase and amplitude engineering, made possible by the degrees of

freedom of the transfer function, tunable enhanced imaging of a point source is numerically demonstrated. First, with unitary transmittance, consider the same focusing phase profile as before. The image distance to the metasurface is given by parameter  $x_0$  and is changed from 60 to 120 mm on figures 11(a) and (b), respectively, thus illustrating how the image position can be tuned. By defining a new transfer function  $H = \gamma C e^{i\phi} - C$ , the wave transmittance and image intensity will become controllable. For example, in figures 11(c) and (d), we select  $\gamma$  to be 5 and 10, respectively, to enhance the image by 5 and 10 times the original one shown in figure 11(b). The normalized out-of-plane displacement field shown in the two figures demonstrate the desired enhancement. In figure 11(e), we extract the magnitude of the normalized out-of-plane displacement field at  $x = 120$  mm (imaging spot). It is seen then that the image intensity is indeed increased nearly to the exact prescribed value.

#### 4.7. Non-reciprocal wave propagation

As another demonstration of the extreme functionalities that the proposed metasurface can achieve, a thin one-way transmitter of flexural waves is realized for the first time. As a matter of fact, the sensing signal,  $V_{in}$ , being dependent on the wave vector, can be designed to break spatial symmetry and reciprocity. For instance, the metasurface can be programmed

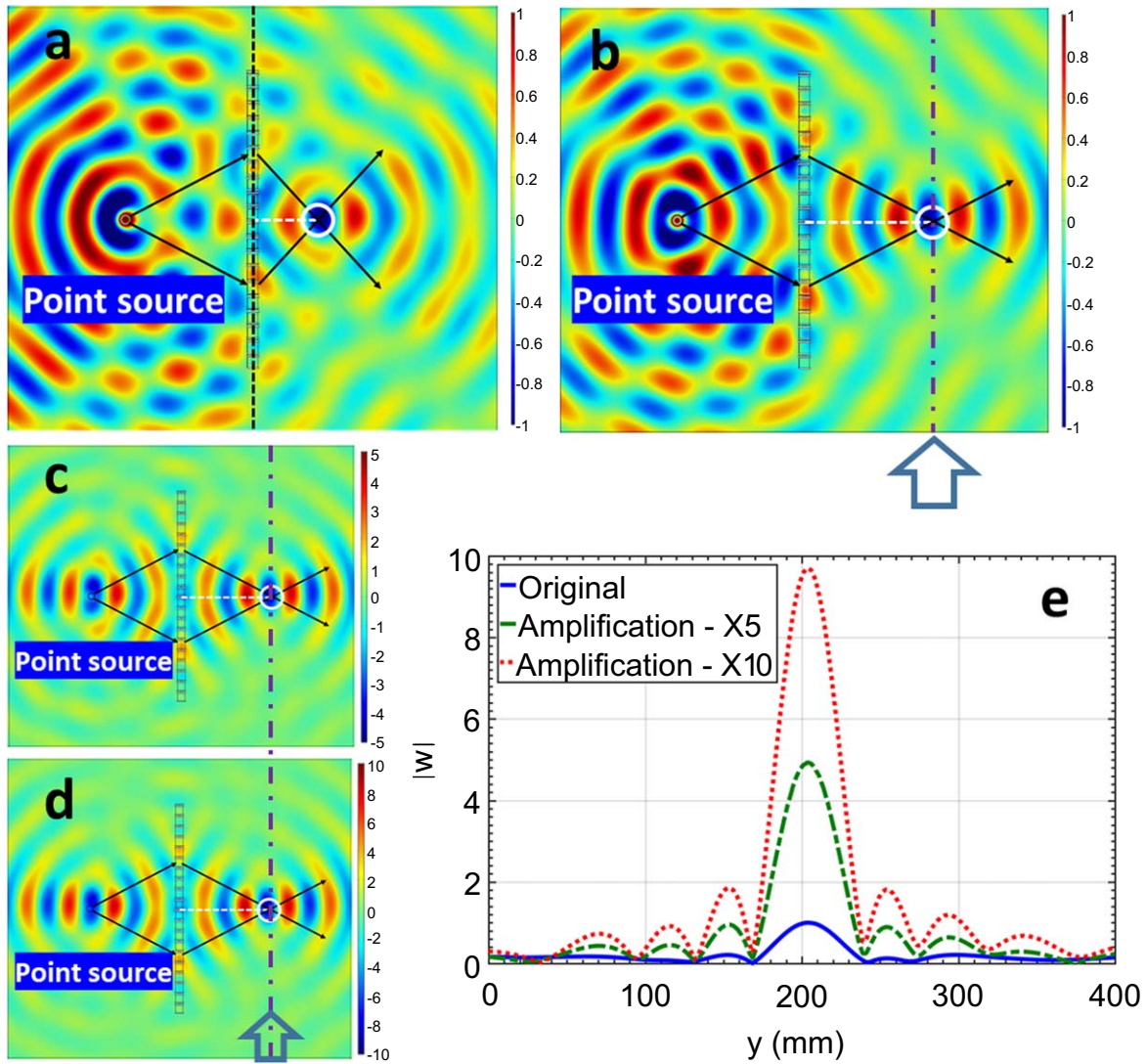


**Figure 11.** Programmable metasurface for enhanced imaging of a point source. (a)–(d) Normalized displacement wave field of the point imaging: (a), (b) at different locations (60 and 120 mm) without amplifications; (c), (d) at the same location (120 mm) with different amplification ratios being 5 and 10; (e) the magnitude of the normalized out-of-plane displacement field at  $x = 120$  mm with different amplification ratios.

to block waves incident from the left while transmitting, or even amplifying, waves incident from the right. Other techniques for breaking reciprocity make use of so-called ‘dynamic materials’ where the constitutive properties need to be constantly changing with time across a depth of multiple wavelengths throughout the bulk of the host medium [43, 44]. In comparison, the suggested metasurface appears as an appealing thin, broadband and reprogrammable substitute. Going into specifics with normal incidences, for the right-going wave, by subtracting the right sensor signal from the left sensor signal, the sensing signal is  $V_{in} = -2i\kappa_s A w_0 \sin(k\delta_d)$ . However, for the left-going wave, the sensing signal is  $V_{in} = 2i\kappa_s A w_0 \sin(k\delta_d)$ , which is out-of-phase with the sensing signal from the right-going wave. Therefore, by adopting the same transfer function,  $H = \frac{1}{2i\kappa_s A \sin(k\delta_d)}$ , the coherent wave fields generated by the actuator in the metasurface will be different:  $w_a = -w_0 e^{ikx}$  in the right-hand-side of the metasurface for right-going incidence; and  $w_a = w_0 e^{-ikx}$  in

the left-hand side of the metasurface for left-going incidence. As a consequence, the right-going wave will be blocked ( $w_r = 0$ ) and the left-going wave is amplified ( $w_l = 2w_0 e^{-ikx}$ ) with an amplitude twice that of the incident wave. Experimental and numerical tests confirm the predicted one-way transmission phenomenon and show good agreement on transmitted waves (see figures 12(a) and (b)). It should be mentioned that, for the case with the right-going incident wave, a standing wave is formed in the region between the source and metasurface. Figure 12(c) shows the numerically calculated amplitude and phase of the displacement for this case, where node points and phase jumps of  $\pi$  are clearly seen. In addition, the wave field in the right-hand-side of the source array in figure 12(b) is approximately expressed as  $w_0 e^{ikx}(1 + e^{i\varphi})$  by summing the incidence and actively-excited waves from the metasurface, where the phase factor  $\varphi$  is determined by the distance between the source and the metasurface,  $L$ , and the wavenumber,  $k$ , as  $\varphi = 2kL$ . In this

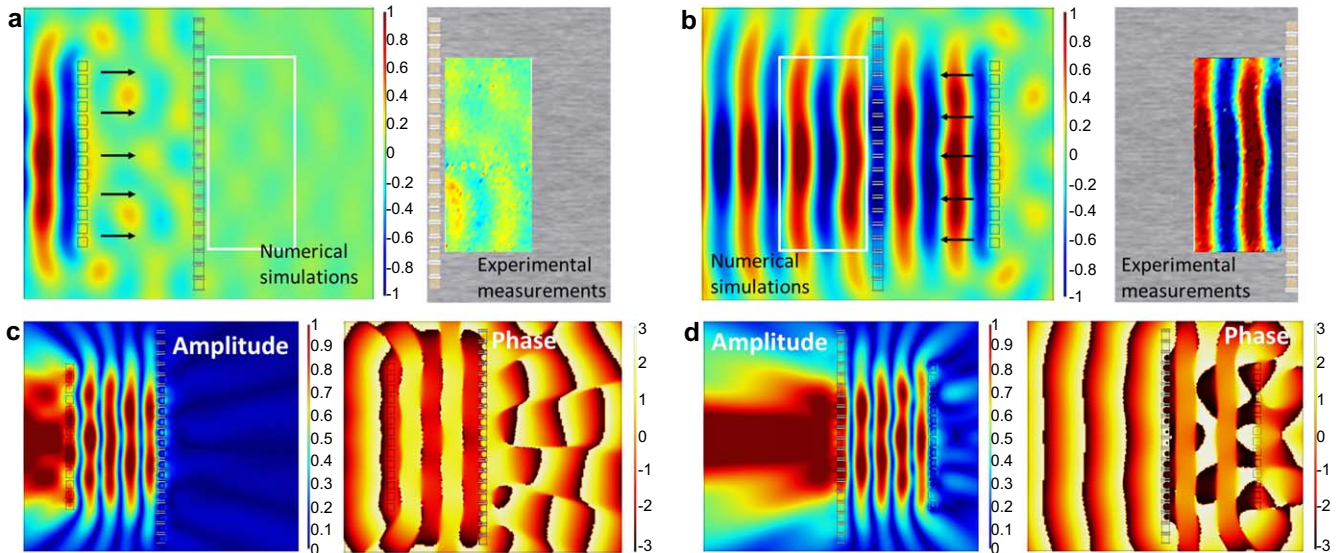


**Figure 12.** One-way wave transmission. (a) Numerically simulated and experimentally measured out-of-plane velocity fields for right-going incident waves. Here, the incident wave is nearly totally blocked; (b) numerically simulated and experimentally measured out-of-plane velocity fields for left-going incident waves. Here, the incident wave is amplified to two times its original amplitude; (c) numerically simulated amplitude and phase of the displacement for right-going incident waves; (d) numerically simulated amplitude and phase of the displacement for left-going incident waves.

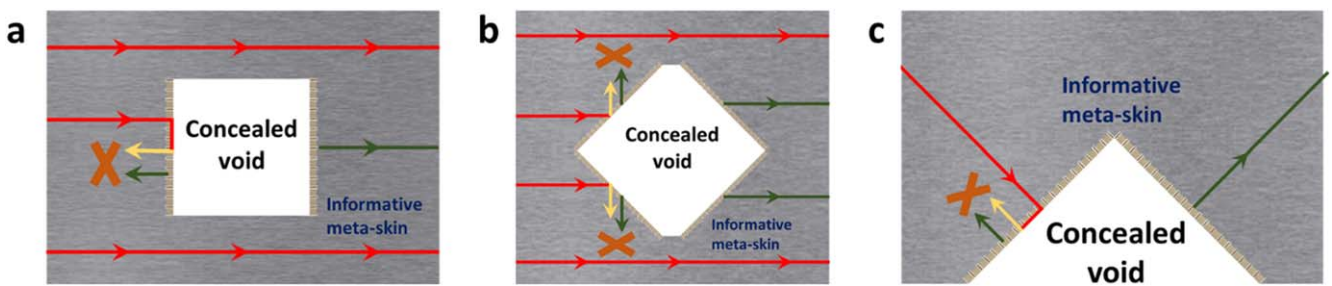


**Figure 13.** Three configurations of skin cloaking of polygonal voids. Red, yellow and green arrowed lines represent incident, reflected and coherent rays, respectively. The perfect destructive wave interference between reflected and coherent waves makes voided boundary facing incident waves reflectionless and effectively invisible. The coherent rays generated on the right metasurface voided boundary makes the voided region invisible to transmitted waves. (a) Skin cloaking of a rectangular void under normal incidence; (b) skin cloaking of a rectangular void under oblique incidence; (c) skin carpet cloaking of a triangular void.

example,  $L = 120$  mm, and  $k = 118$  m<sup>-1</sup>. Finally,  $\varphi = 9\pi$ , producing a near zero wave field in this region, as also shown in figure 12(d) for the amplitude and phase of the displacement.

#### 4.8. Unidirectional skin cloaking of voids

Among the array of applications made possible by the proposed metasurface, the realization of cloaking devices is of particular interest. Cloaking refers to strategies by which scattering by a concealed object is suppressed so that its detection by probing waves becomes impossible. Cloaks, usually passive and omnidirectional, are designed according to one version or another of the transformation method thus requiring the realization of a gradient of material properties across a given distance equal to the thickness of the cloak [45–47]. The present metasurface permits the design of single-layered ultrathin unidirectional cloaks, also referred to as ‘skin cloaks’ [48]. Unidirectional skin cloaking is

demonstrated numerically hereafter in three configurations (see figures 13(a)–(c)). In each configuration, a polygonal portion of the host plate is voided then concealed by a skin cloak. Scattering by the voids is approximated to a good degree of accuracy by reflection occurring on the sides of the voided polygons facing the incident wave. As shown in the figures, each boundary common to both the voided polygons and to the plate and facing the incident wave (red lines) will host a metasurface that will suppress reflections (yellow lines) with coherent waves (green lines). As for the metasurfaces occupying the opposite sides, they will generate a coherent field (green lines) equal to the incident one with a phase delay equal to that the incident field would have acquired had it traveled through the voided region. Thus, the metasurfaces occupying opposite sides need to communicate on a cellular level. Figure 14 shows the three communication configurations between the two metasurfaces occupying opposite sides of voids on this cellular level. For the cases shown in figures 14(a) and (c), the upper (resp. lower) cell in the left

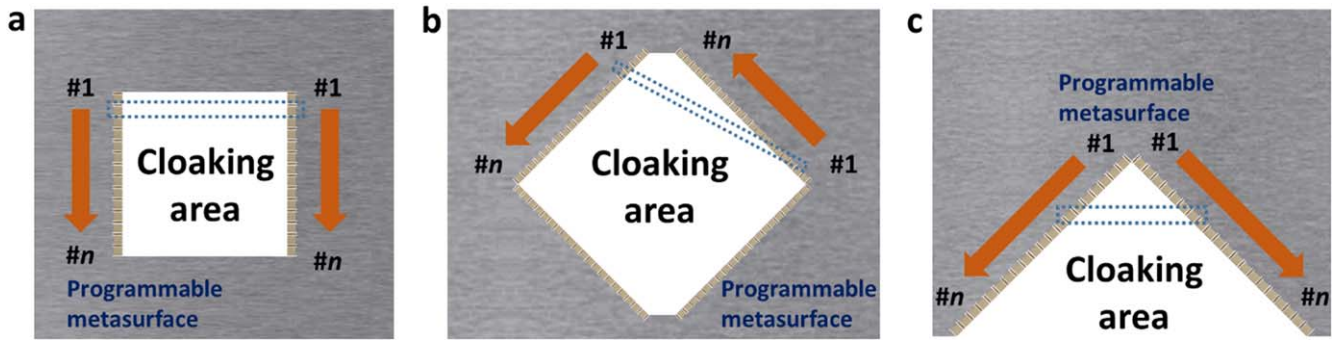


**Figure 14.** Communications on a cellular level for the three skin cloaking configurations. (a) Skin cloaking of a rectangular void under normal incidence; (b) skin cloaking of a rectangular void under oblique incidence; (c) skin carpet cloaking of a triangular void.

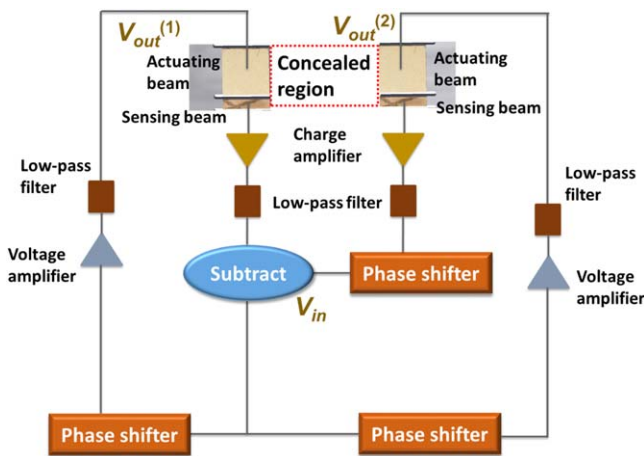


**Figure 15.** Schematic of the feedforward control loop of the metasurface unit cell for invisible cloaks.

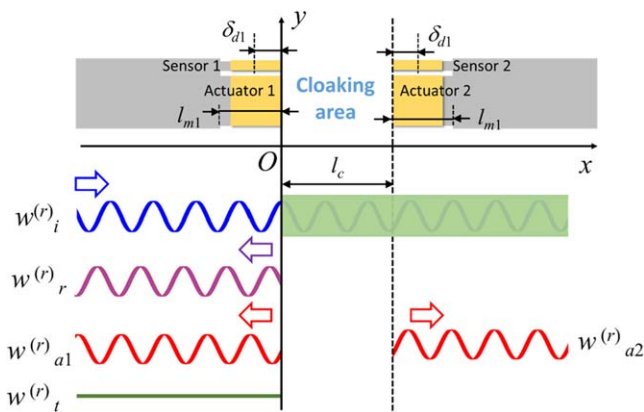


**Figure 16.** Schematic of the one-dimensional harmonic wave analysis of the reflection-type metasurface for invisible cloaks.

metasurface is connected to the upper (resp. lower) cell in the opposing metasurface, composing a new unit cell (dotted rectangles). Note that the cellular communication scheme for oblique incidence (figure 14(b)) is different from the one for normal incidence. As a matter of fact, at oblique incidence, the irradiated (left) metasurface generates a coherent wave that cancels the wave reflected up (figure 13(b)) whereas the opposing metasurface generates a coherent wave traveling to the right (figure 13(b)). Thus, by symmetry, inducing this

effect means that the phase delays among the unit cells of the left and right metasurfaces are identical but listed in an inverse order. Therefore, at oblique incidence, the upper-right (resp. lower-left) cell in the left metasurface is connected to the lower-right (resp. upper-left) cell in the opposing metasurface (dotted rectangle in figure 14(b)).

Figure 15 shows the schematic of the feedforward control loop of the metasurface unit cell for invisible cloaks. The unit cell includes two piezoelectric sensors and two piezoelectric actuators symmetrically bonded on two opposite sides of the concealed region. Sensors and actuators in the unit cell are separated by thin slits and communicated with a control circuit. Two charge amplifiers and two low-pass filters are connected to the two sensors, respectively. Without loss of generality, we assume that the sensor in the left side will sense the incident and reflected wave components and the right-side sensor will not sense either of them because of the concealed region. Thanks to the subtraction operation and the phase shifter on the right-side sensor, the input signal  $V_{in}$  will then feedforward to two actuating beams through two phase shifters. It should be noticed that low-pass filters and voltage amplifiers will be used in the actuating.

In particular, to realize the cloaking, the actively generated elastic waves on both sides should have the same amplitude: one is used to cancel the reflected wave from the cloaked boundary and another one is used to mimic the transmitted or reflected wave field on another side of the cloaked boundary. Physically, the applied voltages on the two actuators,  $V_{out}^{(1)}$  and  $V_{out}^{(2)}$ , should have the same amplitude, and the phase difference between  $V_{out}^{(1)}$  and  $V_{out}^{(2)}$  will be determined by the ray path passing through the two sides of the concealed region. It should be noticed that the coherent wave components among the two sensing signals will possess the same phase difference as those between  $V_{out}^{(1)}$  and  $V_{out}^{(2)}$ . To decouple sensors from actuators by the subtraction operation, the coherent wave components from both sides need to be identical. Therefore, an additional phase shifter for the right-hand side sensor is needed to compensate the phase difference before the subtraction circuit. As a result, the final input signal  $V_{in}$  only contains the incident and reflected wave components and the control loop becomes feedforward.

In this design, the transfer function for unidirectional skin cloaks can be derived based on one-dimensional wave

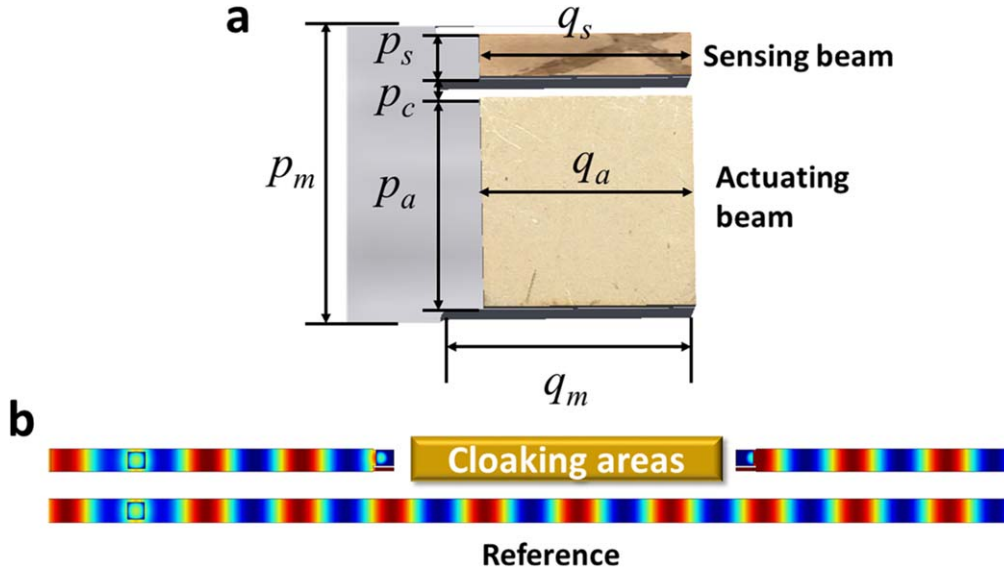


**Figure 17.** (a) Geometric parameters of the reflection-type metasurface unit cell; (b) simulated out-of-plane displacement wave field manipulated by the reflection-type metasurface for invisible cloaks.

**Table 3.** Geometric parameters of the reflection-type programmable metasurface.

$p_s$	2.0 mm	$p_m$	14.0 mm	$q_s$	10.0 mm	$q_m$	12.0 mm
$p_c$	1.0 mm	$p_a$	10.0 mm	$q_a$	10.0 mm		

analysis shown in figure 16, where a unit cell with periodic boundary conditions is selected. Based on same assumptions made in section 2 and considering free boundary conditions at  $x = 0$ , the displacement wave field in the left-side of the metasurface can be expressed as

$$w^{(r)} = w_i^{(r)} e^{ikx} + w_r^{(r)} e^{-ikx} + w_e^{(r)} e^{kx}, \quad (13)$$

where

$$\begin{aligned} w_r^{(r)} &= -iw_i^{(r)}, \\ w_e^{(r)} &= (1 - i)w_i^{(r)}, \end{aligned}$$

with  $w_i^{(r)}$ ,  $w_r^{(r)}$  and  $w_e^{(r)}$  being the complex displacement amplitudes of the incident, and propagated and evanescent reflected waves. It should be mentioned that the coherent wave fields generated by the actuators in the metasurface are not included in equation (13) for the same reason stated in section 2. The input sensing voltage from the subtraction operation can therefore be expressed as

$$V_{in}^{(r)} = (1 - i)\kappa_s A w_i^{(r)} [\cos(k\delta_{d1}) + \sin(k\delta_{d1}) + e^{-k\delta_{d1}}]. \quad (14)$$

In order to make invisible cloaks, the reflected wave should be totally canceled. As a result, the coherent wave field generated by the actuators in the left-side of the metasurface will be

$$w_{a1}^{(r)} = iw_i^{(r)} e^{-ikx}, \quad x < -l_{m1}. \quad (15)$$

Similarly, the wave field generated by the actuators in the right-side of the metasurface is

$$w_{a2}^{(r)} = iw_i^{(r)} e^{ikx} e^{i\Theta}, \quad x > l_c + l_{m1}, \quad (16)$$

where  $\Theta$  is the compensated phase accounted for the concealed region. The coherent wave fields generated by the actuators in both sides of the metasurfaces are assumed to be proportional to the applied voltages but with a phase difference as

$$\begin{aligned} w_{a1}^{(r)} &= \kappa_a V_{out}^{(1)} e^{i\varphi} e^{-ikx}, \quad x < -l_{m1}, \\ w_{a2}^{(r)} &= \kappa_a V_{out}^{(2)} e^{i\varphi} e^{ikx}, \quad x > l_c + l_{m1}. \end{aligned} \quad (17)$$

By comparing equations (15)–(17), the voltages across the actuators should be

$$\begin{aligned} V_{out}^{(1)} &= \frac{iw_i}{\kappa_a e^{i\varphi}}, \\ V_{out}^{(2)} &= \frac{iw_i e^{i\Theta}}{\kappa_a e^{i\varphi}}. \end{aligned} \quad (18)$$

The corresponding transfer functions are

$$\begin{aligned} H^{(1)} &= \frac{(i - 1)}{D e^{i\varphi}}, \\ H^{(2)} &= \frac{(i - 1) e^{i\Theta}}{D e^{i\varphi}}, \end{aligned} \quad (19)$$

where  $D = 2\kappa_a \kappa_s [\cos(k\delta_{d1}) + \sin(k\delta_{d1}) + e^{-k\delta_{d1}}]$ .

In figure 17, numerical simulations are performed to validate the performance of the one-dimensional invisible cloak made by the metasurface at 10 kHz. Geometric parameters are illustrated in figure 17(a) with values listed in table 3. The thickness of the host steel plate is selected as 3.2 mm and the thicknesses of sensor and actuator patches are 1.0 mm and 1.5 mm, respectively. In simulations, the phase,  $\varphi$ , and the constant,  $D$ , in transfer functions are determined numerically. As illustrated in figure 17(b), the out-of-plane displacement wave fields manipulated by the metasurface are almost exact the same with those in a homogeneous plate,

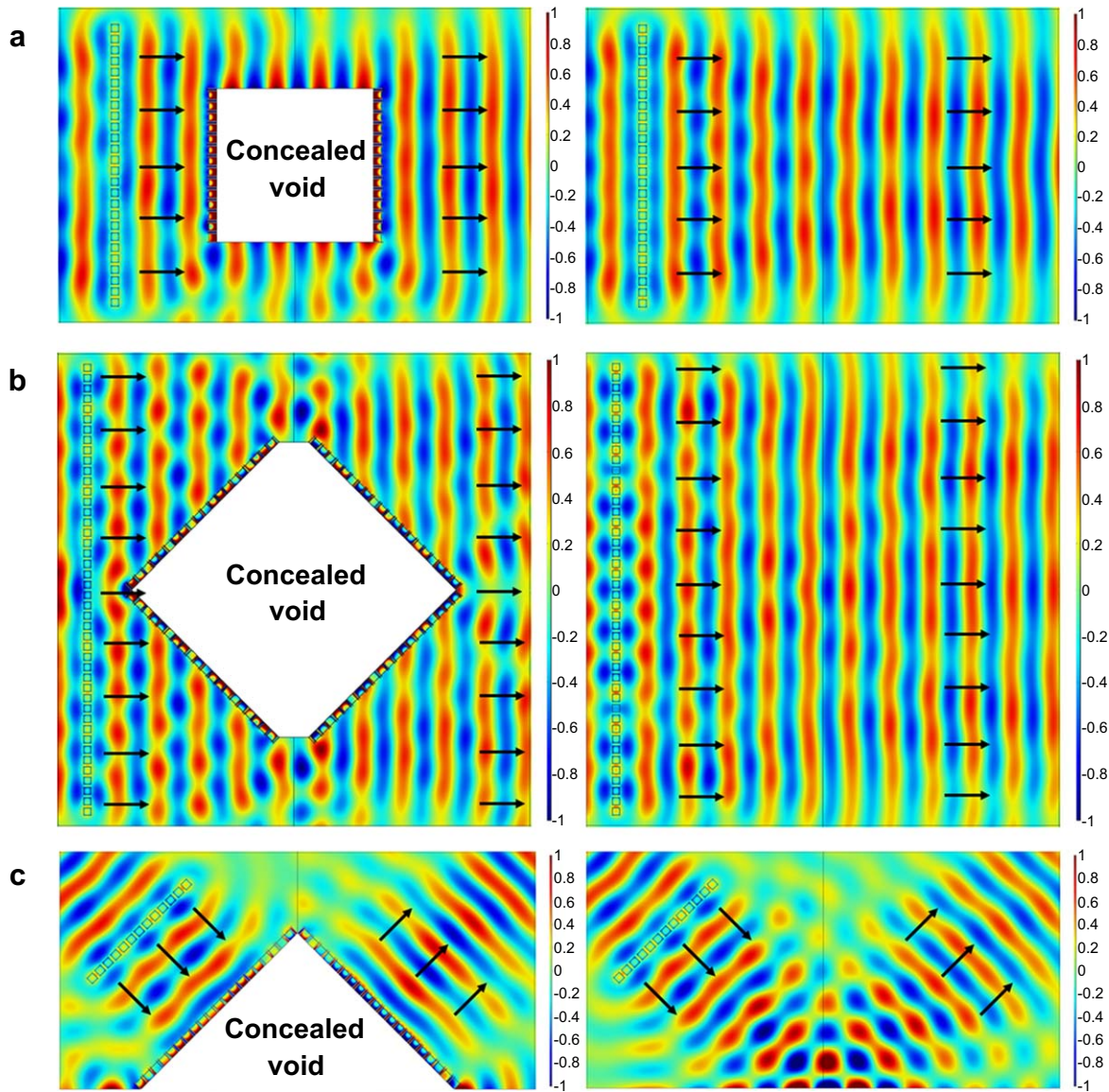


**Figure 18.** Skin cloaking of polygonal voids. (a) Numerical demonstration of skin cloaking of a rectangular void in a plate under normal incidence with the programmable metasurface. (b) Numerical demonstration of skin cloaking of a rectangular void in a plate under oblique incidence with the programmable metasurface; (c) numerical demonstration of skin carpet cloaking of a triangular void on a plate boundary with the programmable metasurface.

which indicates that the voided area is undetectable by using the elastic wave method.

Results of numerical simulations of the three configurations in figures 13(a)–(c) are shown in figures 18(a)–(c). The normalized out-of-plane displacement fields are plotted for right-going incident waves once in the absence of the voided regions and once in their presence, concealed by the proposed skin cloak, at 10 kHz. It can be seen that, in each configuration, fields amplitudes and phases are almost identical with and without the voids thus making the voided regions effectively invisible. The presented cloaking configurations show that the incidence can be normal (see figure 18(a)) or oblique (e.g., at  $45^\circ$ , figure 18(b)). Further, the cloaked region can occupy the boundary of the plate. The situation depicted in figure 18(c), illustrates a skin carpet cloak. The major difference here is that the cloak needs to compensate for the

reflections along the boundary of the plate that would have occurred in the absence of the voids. Here too, figure 18(c) shows that the displacement fields in the presence and absence of the voids are almost identical in terms of amplitude and phase. Note that in cloaking applications, the metasurface is highly efficient energetically since all energy radiated from the metasurface is exploited. Although the underlying metasurface concept is the same, the experimental set-up for skin cloaking has significant differences in comparison to the one used before, which therefore has not been demonstrated here. It may be noted that the invisibility cloaks designed here based on the programmable metasurface are not perfect since, for instance, prior knowledge of the incidence angle is required, the approach, however, remains highly appealing given its simplicity and the extremely small thickness of the designed cloaks.

## 5. Conclusion

The suggested programmable elastic metasurface with self-sensing-and-actuating units provides an appealing platform for real-time, multifunctional and asymmetric trajectory control of elastic waves. By simply programming electric circuits, we were able, for the first time, to control in real time the ray paths of transmitted signals, be them rectilinear or curvilinear. In addition, by selecting particular transfer functions, the design can support one-way non-reciprocal wave blocking as well as cloaking functionalities. These are but a few examples of the range of functions that the programmable metasurface can achieve. The presented approach can be extended to different time and length scales and to different wave systems. The immediate applications of the concept we foresee are related to stealth technology, active noise control and the realization of ideal experimental platforms with isolated or otherwise controlled environments.

## Acknowledgments

This work is supported by the Air Force Office of Scientific Research under Grant No. AF 9550-18-1-0342 with Program Manager Dr Byung-Lip (Les) Lee and the NSF EFRI under award No. 1641078. The support from National Natural Science Foundation of China (Grant No. 11632003) is also acknowledged.

## ORCID iDs

Guoliang Huang  <https://orcid.org/0000-0003-0959-8427>

## References

- [1] Pao Y H 1983 Elastic waves in solids *J. Appl. Mech.* **50** 1152–64
- [2] Li J and Rose J L 2001 Implementing guided wave mode control by use of a phased transducer array *IEEE Trans. Ultrason. Ferroelectr. Freq. Control* **48** 761–8
- [3] Drinkwater B W and Wilcox P D 2006 Ultrasonic arrays for non-destructive evaluation: a review *NDT Int.* **39** 525
- [4] Cummer S A, Christensen J and Alù A 2016 Controlling sound with acoustic metamaterials *Nat. Rev. Mater.* **1** 16001
- [5] Ma G and Sheng P 2016 Acoustic metamaterials: from local resonances to broad horizons *Sci. Adv.* **2** e1501595
- [6] Hussein M I, Leamy M J and Ruzzene M 2014 Dynamics of phononic materials and structures: historical origins, recent progress and future outlook *Appl. Mech. Rev.* **66** 040802
- [7] Liu Z Y, Zhang X, Mao Y, Zhu Y Y, Chan C T and Sheng P 2000 Locally resonant sonic materials *Science* **289** 1734
- [8] Haberman M and Guild M 2016 Acoustic metamaterials *Phys. Today* **69** 42
- [9] Fang N, Xi D, Xu J, Ambati M, Srituravanich W, Sun C and Zhang X 2006 Ultrasonic metamaterials with negative modulus *Nat. Mater.* **5** 452
- [10] Zhu R, Liu X N, Hu G K, Sun C T and Huang G L 2014 Negative refraction of elastic waves at the deep subwavelength scale in a single-phase metamaterial *Nat. Commun.* **5** 5510
- [11] Bergamini A E, Delpero T, Simoni L D, Lillo L D, Ruzzene M and Ermanni P 2014 Phononic crystal with adaptive connectivity *Adv. Mater.* **9** 1343
- [12] Chen Y Y, Hu G K and Huang G L 2016 An adaptive metamaterial beam with hybrid shunting circuits for extremely broadband control of flexural waves *Smart Mater. Struct.* **25** 105036
- [13] Zhu R, Chen Y Y, Barnhart M V, Hu G K, Sun C T and Huang G L 2016 Experimental study of an adaptive elastic metamaterial controlled by electric circuits *Appl. Phys. Lett.* **108** 011905
- [14] Chen Y Y, Zhu R, Barnhart M V and Huang G L 2016 Enhanced flexural wave sensing by adaptive gradient-index metamaterials *Sci. Rep.* **6** 35048
- [15] Celli P and Gonella S 2015 Tunable directivity in metamaterials with reconfigurable cell symmetry *Appl. Phys. Lett.* **106** 091905
- [16] Chen Y Y, Hu J and Huang G L 2016 A design of active elastic metamaterials for control of flexural waves using the transformation method *J. Intell. Mater. Syst. Struct.* **27** 1337
- [17] Chen Y Y, Hu G K and Huang G L 2017 A hybrid elastic metamaterial with negative mass density and tunable bending stiffness *J. Mech. Phys. Solids* **105** 179
- [18] Wang G, Cheng J, Chen J and He Y 2017 Multi-resonant piezoelectric shunting induced by digital controllers for subwavelength elastic wave attenuation in smart metamaterial *Smart Mater. Struct.* **26** 025031
- [19] Li X, Chen Y, Hu G and Huang G 2018 A self-adaptive metamaterial beam with digitally controlled resonators for subwavelength broadband flexural wave attenuation *Smart Mater. Struct.* **27** 045015
- [20] Li S, Xu J and Tang J 2018 Tunable modulation of refracted lamb wave front facilitated by adaptive elastic metasurfaces *Appl. Phys. Lett.* **112** 021903
- [21] Hsiao H H, Chu C H and Tsai D P 2017 Fundamentals and applications of metasurfaces *Small Methods* **1** 1600064
- [22] Yu N, Genevet P, Kats M A, Aieta F, Tetienne J P, Capasso F and Gaburro Z 2011 Light propagation with phase discontinuities: generalized laws of reflection and refraction *Science* **334** 333
- [23] Lin D, Fan P, Hasman E and Brongersma M L 2014 Dielectric gradient metasurface optical elements *Science* **345** 298
- [24] Zhang L, Mei S, Huang K and Qiu C 2016 Advances in full control of electromagnetic waves with metasurfaces *Adv. Opt. Mater.* **4** 818
- [25] Chen K *et al* 2017 A reconfigurable active Huygens' metasurfaces *Adv. Mater.* **29** 1606422
- [26] Xie Y, Wang W, Chen H, Konneker A, Popa B I and Cummer S A 2014 Wavefront modulation and subwavelength diffractive acoustics with an acoustic metasurface *Nat. Commun.* **5** 5553
- [27] Li Y, Jiang X, Li R Q, Liang B, Zou X Y, Yin L L and Cheng J C 2014 Experimental realization of full control of reflected waves with subwavelength acoustic metasurfaces *Phys. Rev. Appl.* **2** 064002
- [28] Mei J and Wu Y 2014 Controllable transmission and total reflection through an impedance-matched acoustic metasurface *New J. Phys.* **16** 123007
- [29] Memoli G, Caleap M, Asakawa M, Sahoo D R, Drinkwater B W and Subramanian S 2017 Metamaterial bricks and quantization of meta-surfaces *Nat. Commun.* **8** 14608
- [30] Popa B I, Shinde D, Konneker A and Cummer S A 2015 Active acoustic metamaterials reconfigurable in real time *Phys. Rev. B* **91** 220303

- [31] Zhu H and Semperlotti F 2016 Anomalous refraction of acoustic guided waves in solids with geometrically tapered metasurfaces *Phys. Rev. Lett.* **117** 034302
- [32] Su X and Norris A 2016 Focusing, refraction, and asymmetric transmission of elastic waves in solid metamaterials with aligned parallel gaps *J. Acoust. Soc. Am.* **139** 3386
- [33] Liu Y, Liang Z, Liu F, Diba O, Lamb A and Li J 2017 Source illusion devices for flexural Lamb waves using elastic metasurfaces *Phys. Rev. Lett.* **119** 034301
- [34] Zhu B O, Zhao J and Feng Y 2013 Active impedance metasurface with full 360° reflection phase tuning *Sci. Rep.* **3** 3059
- [35] Cui T J, Qi M Q, Wan X, Zhao J and Cheng Q 2014 Broadband diffusion of terahertz waves by multi-bit coding metasurfaces *Light Sci. Appl.* **3** e218
- [36] Liu S and Cui T J 2017 Flexible controls of terahertz waves using coding and programmable metasurfaces *IEEE J. Sel. Top. Quantum Electron.* **23** 1
- [37] Popa B I and Cummer S A 2014 Non-reciprocal and highly nonlinear active acoustic metamaterials *Nat. Commun.* **5** 3398
- [38] de Pineda J D, Mitchell-Thomas R C, Hibbins A P and Sambles J R 2017 A broadband metasurface Luneburg lens for microwave surface waves *Appl. Phys. Lett.* **111** 211603
- [39] Jia S L, Wan X, Su P, Zhao Y J and Cui T J 2016 Broadband metasurface for independent control of reflected amplitude and phase *AIP Adv.* **6** 045024
- [40] Wang Q, Zhang X, Xu Y, Gu J, Li Y, Tian Z, Singh R, Zhang S, Han J and Zhang W 2016 Broadband metasurface holograms: toward complete phase and amplitude engineering *Sci. Rep.* **6** 32867
- [41] Wen D *et al* 2015 Helicity multiplexed broadband metasurface holograms *Nat. Commun.* **6** 8241
- [42] Devlin R C, Khorasaninejad M, Chen W T, Oh J and Capasso F 2016 Broadband high-efficiency dielectric metasurfaces for the visible spectrum *Proc. Natl Acad. Sci. USA* **113** 10473
- [43] Nassar H, Xu X C, Norris A N and Huang G L 2017 Modulated phononic crystals: non-reciprocal wave propagation and Willis materials *J. Mech. Phys. Solids* **101** 10
- [44] Nassar H, Chen H, Norris A N, Haberman M R and Huang G L 2017 Non-reciprocal wave propagation in modulated elastic metamaterials *Proc. R. Soc. A* **473** 20170188
- [45] Pendry J B, Shurig D and Smith D R 2006 Controlling electromagnetic fields *Science* **312** 1780
- [46] Chen Y, Zheng M, Liu X, Bi Y, Sun Z, Xiang P, Yang J and Hu G 2017 Broadband solid cloak for underwater acoustics *Phys. Rev. B* **95** 180104
- [47] Farhat M, Guenneau S and Enoch S 2009 Ultrabroadband elastic cloaking in thin plates *Phys. Rev. Lett.* **103** 024301
- [48] Ni X, Wong Z J, Mrejen M, Wang Y and Zhang X 2015 An ultrathin invisibility skin cloak for visible light *Science* **349** 1310